Mapping the intramolecular contributions to the inelastic electron tunneling signal of a molecular junction

Giuseppe Foti[*] and Héctor Vázquez[†]

Institute of Physics, Academy of Sciences of the Czech Republic, Cukrovarnicka 10, Prague, Czech Republic
(Received 29 April 2016; published 12 July 2016)

We present a quantitative analysis of the intramolecular origin of the inelastic electron tunneling signal of a molecular junction. We use density-functional theory to study a representative conjugated molecule with a low degree of symmetry and calculate, for all modes, the different contributions that give rise to the vibrational spectrum. These local contributions involve products of scattering states with electron-phonon matrix elements and thus encode information on both the vibrational modes and the electronic structure. We separate these intra- and interatomic terms and draw a pattern of addition or cancellation of these partial contributions throughout the inelastic spectrum. This allows for a quantitative relation between the degree of symmetry of each vibrational mode, its inelastic signal, and the locality of selection rules.

I. INTRODUCTION

The interaction of tunneling electrons with localized vibrations in molecular junctions has important implications not only in terms of conductance but also for the stability and dynamics of the system under an applied bias. Inelastic electron tunneling spectroscopy (IETS) has been studied to monitor or induce chemical reactions and conformational changes of molecular adsorbates [1–3] or for the real-space imaging of molecular structure [4]. In the field of molecular electronics, vibrational spectroscopy based on IET is successfully employed for the chemical and structural identification of the junction [5–13]. Compared to elastic transport, the interaction of the tunneling electrons with vibrational degrees of freedom enables additional channels for conductance. This results in the appearance of peaks or dips in the second derivative of current with respect to bias at the threshold of mode energies [14–17]. Theoretical analyses based on *ab initio* simulations of the inelastic electron tunneling process [18–22] provide atomic-scale resolution for the study of intramolecular contributions to the inelastic signal. Knowing whether and how electrons interact with molecular vibrations is not always trivial. Previous works have formulated and explored the propensity rules governing the generation of the inelastic signal [17,23–27]. The probability of having inelastic scattering between an initial and a final state coming from the left and right electrodes due to a particular vibrational mode has been expressed in the form of a Fermi golden rule where the deformation potential associated to the vibrational mode couples the two states [17]. In particular, a mode is active if the coupling between the two scattering states due to the deformation potential is nonzero. For instance, for a CO molecule with its rotational axis coinciding with the transport direction, scattering channels of π symmetry would interact only with vibrational longitudinal modes to give an inelastic signal [26]. If only one of the left- or right-propagating channels has σ symmetry, no longitudinal modes will appear in the IETS. These rules have successfully explained the intensity of IETS peaks for relatively small molecules with a well-defined

symmetry [17,25,26]. For more general molecular structures with a low degree of symmetry, however, the application of these propensity rules can be more involved. For these cases, in fact, symmetry considerations should be supplemented by an analysis of the current pathway [24]. A mode could locally satisfy symmetry considerations yet have a low signal because of the destructive interactions between different regions of the molecule. Thus, a general distinction between active and dark (inactive) modes becomes less trivial. A systematic study in terms of local contributions for all vibrational modes provides a powerful tool to disentangle the submolecular origin of IETS.

In this paper, we carry out such analysis and generalize the previous approaches in a method to explore the local contributions to the inelastic signal. By taking advantage of a localized basis set representation of the Hamiltonian and the electron-phonon coupling matrix, we completely characterize the origin and intramolecular contributions to the inelastic electron tunneling signal over the whole energy spectrum. We decompose the total signal into the sum of intra- and interatomic contributions and separate those coming from the molecule from those associated to the metal layers. We illustrate this method by considering a molecular junction where a conjugated ring is anchored to gold electrodes through CH_2-S-CH_3 groups, a representative example of a conjugated molecule having metal-molecule bonds with a low degree of symmetry.

This analysis integrates vibrational and electronic structure information to create a real-space mapping of the contributions to all inelastic modes. This allows for the characterization beyond the IET spectra (where the peak heights correspond to the total signal of each mode, regardless of its individual contributions) and the plots of vibrational modes (which do not contain any information about the relevant scattering states).

We can then elucidate, across all vibrational modes, the intramolecular generation of the inelastic signal for active modes and the absence of a signal for dark modes, establishing a connection between the intensity of the inelastic signal, the degree of symmetry of the vibrational modes, and the locality of inelastic propensity rules.

II. GEOMETRIES AND COMPUTATIONAL DETAILS

The elastic and inelastic transport properties of benzenes with thiol- or amine-anchoring groups have been extensively
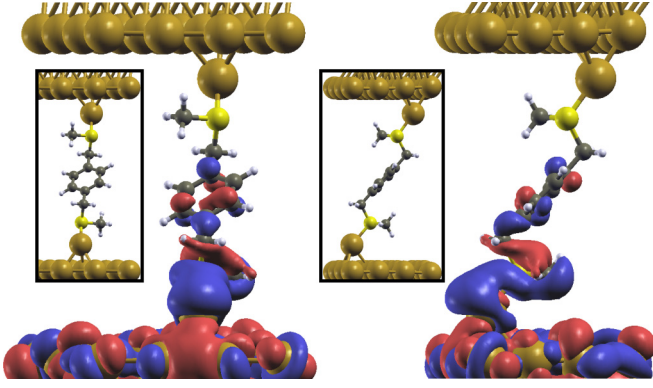
---

*foti@fzu.cz
†vazquez@fzu.cz

FIG. 1. Front and side view of the most transmitting eigenchannel. The inset shows the front and side view of the molecular junction.

FIG. 2. Inelastic signal as a function of energy. The inset shows the high-energy part of the spectrum.

studied both theoretically and experimentally [24,25,28–32]. Here we consider a more general case where a benzene ring is anchored to Au(111) electrodes through CH_2-S-CH_3 linker groups [33]. The insets in Fig. 1 show a front and side view of the junction. Linkers bind to the Au surface through an adatom on both sides of the junction.

We use SIESTA [34] and TRANSIESTA [35] for the structure relaxation and the calculation of the electronic and transport properties. We use a single-ζ plus polarization basis for gold and a double-ζ plus polarization basis for sulfur, hydrogen, and carbon atoms. Exchange-correlation is described with the generalized gradient approximation (GGA) [36]. For the calculation of the electron-phonon coupling matrix we use the INELASTICA code [19] with the $\mathbf{M}(\Gamma)$ approximation [37], which consists in calculating the electron-phonon coupling matrix $\mathbf{M}$ in just one point of the Brillouin zone (Γ) for both electrons and phonons.

The position of the molecule, tip atoms, and the surface gold layers were relaxed until residual forces fell below $0.02 \, \text{eV/Å}$. We used a $k = 5 \times 5 \times 1$ Monkhorst-Pack grid for the calculation of the electronic structure. Eigenchannels are calculated following the method of Paulsson and Brandbyge [38]. Figure 1 shows a front and side view of the most transmitting eigenchannel. The nonplanar structure of the molecule and the presence of bulky linker groups lower the symmetry of the scattering channel. While it locally has σ-type symmetry on the anchoring groups, on the benzene ring it becomes π-type. In the following we restrict our analysis to this most conducting eigenchannel since the second-most conducting channel has a much lower transmission (at the Γ point, $T_1(E_F) = 1.6 \times 10^{-4}$ and $T_2(E_F) = 1.0 \times 10^{-7}$). We reduced further the computational cost of the calculation by applying the wide band approximation (WBA) [18,39], where one assumes that the density of states (DOS) of both electrodes and molecule around Fermi level is constant over the energy range defined by the vibrational frequencies ($\sim$400 meV).

III. RESULTS

A. Inelastic signal and local contributions

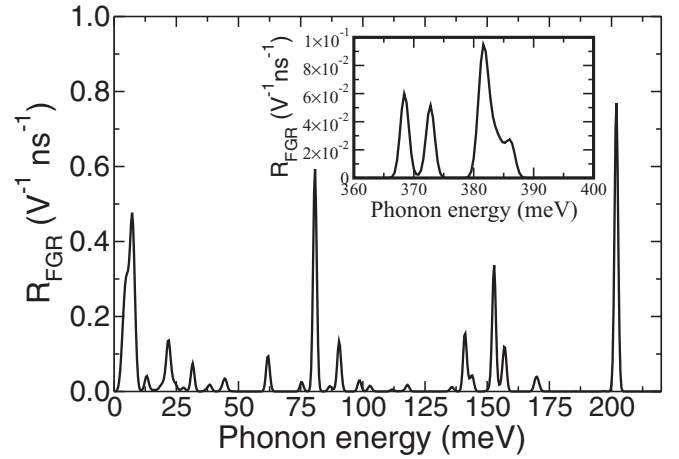In previous works, propensity rules governing the inelastic scattering of tunneling electrons in molecular junctions [23–27] have been formulated in terms of left/right-propagating scattering states and the electron-vibration coupling matrix $M_{e\text{-ph}}^{\lambda}$ [17]:

$$
\begin{aligned}
R_{\text{FGR}}^{\lambda} &= \frac{4\pi e}{\hbar} \left| \langle \Psi_L | M_{e\text{-ph}}^{\lambda} | \Psi_R \rangle \right|^2 \\
&= \frac{4\pi e}{\hbar} \left| \gamma_{\text{tot}}^{\lambda} \right|^2,
\end{aligned} \tag{1}
$$

where λ denotes a vibrational mode. The eigenchannels can be expressed in terms of basis functions (atomic orbitals) ϕ_n as follows:

$$
\Psi_{L,R} = \sum_n C_n^{L,R} | \phi_n \rangle, \tag{2}
$$

where the coefficients $C_n^{L(R)}$ are calculated from the transmission matrix in the basis of the eigenvectors of the left (right) spectral functions [38]. Figure 2 shows the inelastic rates [Eq. (1)] as a function of energy for all vibrational modes.

The low-energy part of the spectrum (below 50 meV) is dominated by vibrational modes of the Au atoms of the electrodes and of the metal-molecule contact [19,40,41]. The peaks above 50 meV are associated to the *adatom-molecule-adatom* complex. Figure 2 has three main peaks at 81, 153, and 202 meV. The modes at 153 and 202 meV are characterized by the stretching of the benzene C-C bonds and the benzene-methyl bonds, at energies close to what was found in previous works for benzenedithiols (BDT) [31,40]. The peak at 81 meV is characterized by the stretching of the S-C bond, while for BDT on Au, a peak associated to an out-of-plane aryl bending mode is found at 97 meV [31,40].

Above 365 meV we find a group of modes giving a smaller inelastic signal. Usually, these high-energy peaks are associated to the C-H stretching modes of the CH_3 groups [12] but, as will be shown later, more contributions have to be taken into account to properly describe this part of the spectrum. Using Eq. (2) we now write the (dimensionless) quantity $\gamma_{\text{tot}}^{\lambda}$ as

$$
\gamma_{\text{tot}}^{\lambda} = \sum_{m,n} C_m^{L\dagger} M_{m,n}^{\lambda} C_n^R, \tag{3}
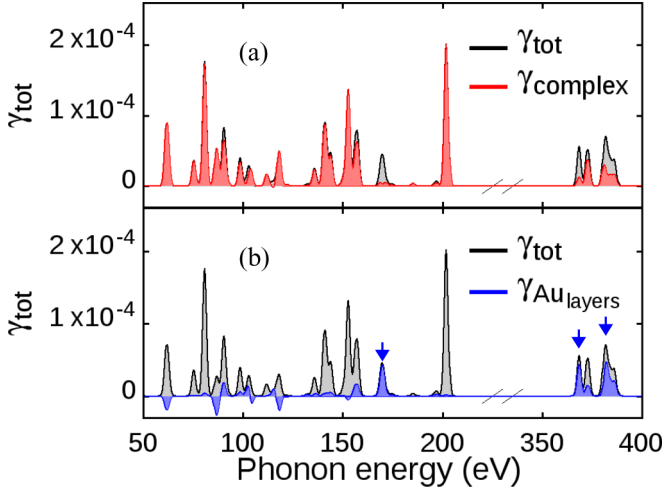$$

FIG. 3. Comparison of the total inelastic signal (black) with (a) the signal originating on the adatom-molecule-adatom complex only (red) and (b) signal involving orbitals of the Au layers (blue). Arrows indicate the peaks for which these contributions are particularly important.

and group all the contributions according to the atoms the orbitals belong to:

$$\gamma_{\text{tot}}^{\lambda} = \sum_{\alpha,\beta} \gamma_{\alpha,\beta}^{\lambda}$$
$$= \gamma_{1,1}^{\lambda} + \gamma_{1,2}^{\lambda} + \gamma_{1,3}^{\lambda} + \dots \gamma_{2,1}^{\lambda} + \gamma_{2,2}^{\lambda} + \gamma_{2,3}^{\lambda} + \dots, \quad (4)$$

with α,β atom indices. For example, the interatomic contribution $\gamma_{1,2}^{\lambda}$ is given by the sum of the terms involving orbitals on atom 1 with orbitals on atom 2. As exemplified below, we find it useful to separate these atomic contributions into the sum of the following two terms:

$$\gamma_{\text{tot}}^{\lambda} = \gamma_{\text{complex}}^{\lambda} + \gamma_{\text{Au layers}}^{\lambda}. \quad (5)$$

The first term $\gamma_{\text{complex}}^{\lambda}$ is generated on the adatom-molecule-adatom complex. It is given by the sum of the terms involving the orbitals of this complex only. The second term includes the remaining contributions, which correspond to orbitals of the Au layers only or orbitals of the Au layers and of the molecular complex. The role of $\gamma_{\text{Au layers}}^{\lambda}$ will be discussed in Sec. III F.

Figure 3(a) shows a comparison between the total signal and the one coming from the molecular complex alone. It can be seen that, except for a few modes that we discuss later, $\gamma_{\text{complex}}^{\lambda}$ is a good approximation for most of the high-intensity peaks in the energy range between 50 and 400 meV, corroborating the intuitive idea that IETS can be used for chemical identification.

In the following sections we drop the λ superscript from the γ terms to alleviate the notation.

B. Cancellation pattern

In Eq. (4) the total signal is expressed as the sum of atomic contributions. The sign and amplitude of each contribution determines whether the final value of γ_{tot} is high (active mode) or low (dark mode). Following Gagliardi *et al.* [25], we define a cancellation parameter δ for each mode measuring how much the different contributions on the molecular complex sum up
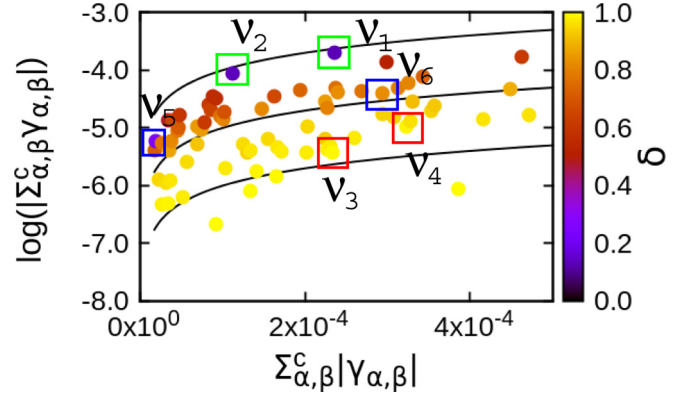

FIG. 4. Correlation plot of the absolute value of the sum of contributions, the sum of the absolute values of the contributions, and cancellation parameter δ for all vibrational modes.

or cancel each other out in that mode,

$$\delta = 1 - \frac{\left| \sum_{\alpha,\beta}^{c} \gamma_{\alpha,\beta} \right|}{\sum_{\alpha,\beta}^{c} |\gamma_{\alpha,\beta}|}, \quad (6)$$

where the superscript c means that the sum is restricted to the molecular complex. When $\delta = 1$ all contributions cancel out completely. Conversely, when $\delta = 0$ all contributions sum up with the same sign and no cancellation takes place. In the expression for δ we consider the pairs of contributions summing up to the 99% of the signal originating from the molecular complex. This allows us to exclude from the analysis the smaller contributions affecting the value of δ but not γ_{complex}. We will come back to this point later.

We now look in detail into the addition or cancellation of the inelastic signal in the adatom-molecule-adatom complex. To do this, we compare the absolute value of the sum of contributions ($| \sum_{\alpha,\beta}^{c} \gamma_{\alpha,\beta}|$) with the sum of the absolute values of the contributions ($\sum_{\alpha,\beta}^{c} |\gamma_{\alpha,\beta}|$). Figure 4 plots the logarithm of the first quantity versus the second one for all 84 vibrational modes. Notice that, for each mode, the quantity on the y axis gives a measure of the inelastic signal $|\gamma_{\text{complex}}|$, while the quantity in the x axis represents what the signal on the molecular complex would be if all contributions were of the same sign and added up. The color bar shows the value of the cancellation parameter. The figure also shows three lines corresponding to $y = x$, $y = x/10$, and $y = x/100$, whose purpose is to serve as guides to the eye to give an idea of the degree of cancellations present in each mode.

From Fig. 4 it is clear that, for most modes, there are many cancellations taking place. In fact, only two modes in Fig. 4 (ν_1 and ν_2) are close to the $y = x$ curve, which corresponds to no cancellations. Many modes are close to the $y = x/10$ curve, and several modes are close to the $y = x/100$ curve, where only 1% of the contributions survive to yield an inelastic signal. Thus, for most modes, local contributions tend to cancel each other, making the total signal substantially smaller than the simple sum of contributions with the same sign. When considering the cancellation parameter δ, we can identify, despite a rather large dispersion, a general trend. Modes with high δ give a weak signal. On the other hand, a small value of δ is associated to a large total signal [25]. The magnitude
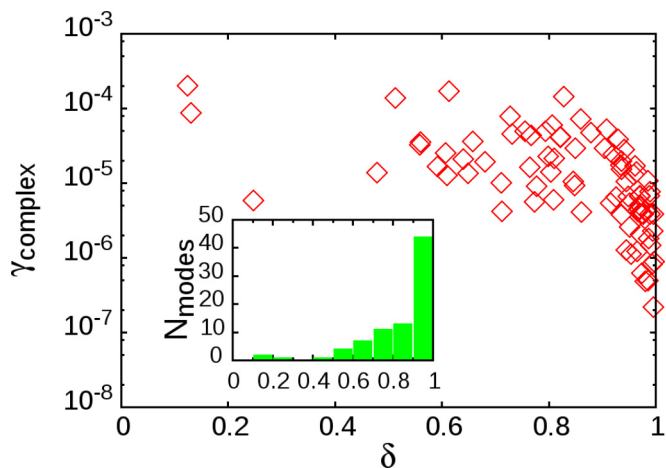
FIG. 5. Inelastic signal generated on the molecular complex $\gamma_{complex}$ as a function of the cancellation parameter δ. The inset shows a histogram of δ.

TABLE I. Energy, description, and symmetry parameter S_λ for the six modes in Fig. 4.

Mode label	Energy (meV)	Type	S_λ
ν_1	202 meV	Symm	−0.24
ν_2	142 meV	Symm	−0.20
ν_3	185 meV	Antisymm	0.29
ν_4	92 meV	Antisymm	0.28
ν_5	384 meV	Asymm	0.00
ν_6	22 meV	Asymm	−0.03

of the total signal also depends on the absolute values of the individual contributions: for the same cancellation parameter (color), larger terms ($\sum_{\alpha,\beta}^c |\gamma_{\alpha,\beta}|$) can result in a larger sum ($|\sum_{\alpha,\beta}^c \gamma_{\alpha,\beta}|$).

To examine the relation between the inelastic signal generated on the molecular complex and the cancellation parameter, we plot on Fig. 5 $\gamma_{complex}$ as a function of δ. Although there is a clear dependence, $\gamma_{complex}$ does not follow a simple relation with respect to δ. Also, as shown by the histogram in the inset, there is a strong accumulation of points (modes) close to $\delta = 1$, which means that most modes have a high cancellation parameter. In this first-principles description of the molecular junction, we find that there are many contributions, most of which are very small. These tend to skew the histogram toward 1. δ was calculated sorting the contributions in decreasing order and truncating them when the sum reached 99% of the total, as mentioned in the previous section. However, even thus removing many (very small) contributions we see that most modes exhibit a high value of δ. Removing this truncation and including all contributions shifts the histogram toward $\delta = 1$ even more. We find that this skew of the histogram is a consequence of the realistic description (double-ζ polarized) of the atomic basis in the calculations, where many (small) local contributions are generated. Figure 5 shows that, for this molecular junction, a higher inelastic signal corresponds to a low-cancellation parameter, an intuitive result in agreement with previous studies [25]. However, the large scatter in Fig. 5 suggests that the inelastic signal in this system can be better characterized by some other parameter, which we introduce in Sec. III D.

C. Real-space local contribution plots

The intra- and interatomic local contributions $\gamma_{\alpha,\alpha}$, $\gamma_{\alpha,\beta}$ to the inelastic signal can be plotted to give a visual representation of the contribution pattern to each vibrational mode. We illustrate this for several modes. These modes are marked in Fig. 4 and their properties are listed in Table I. These six examples are representative of the different modes we find for this system.

Figure 6 shows the local contribution plots for modes ν_1 (a) and ν_2 (b). As seen in Fig. 4, these are active modes and result in high-intensity peaks. The lower panels illustrate the vibrational modes. The arrows represent the amplitudes of the eigenvectors ($\mathbf{v}^\lambda$) of the dynamical matrix on each atom. The top panels show a schematic of the adatom-molecule-adatom structure depicting the local contributions of that mode. The color of each circle (line) corresponds to the value of the intraatomic $\gamma_{\alpha,\alpha}$ (interatomic $\gamma_{\alpha,\beta}$) element. Since nonnearest neighbor interatomic contributions are much smaller than nearest-neighbor ones, only the latter are represented. The figure also quotes the cumulative contributions of each mode [γ_{tot}, Eq. (4)] and the value of the cancellation parameter δ. To simplify the visualization, CH_3 groups are drawn as bigger dots and with a thicker line and the contributions on the CH_3 groups are summed without loss of generality.

The added value of these real-space plots of the inelastic local contributions is that they go beyond the simple visualization of the vibrational modes (lower panels) since they encode information not only of the forces acting on the atoms but also on the electronic part through the electron-phonon coupling matrix and the eigenchannels. This convolution of vibrational and electronic properties cannot be deduced by inspecting the vibrational modes alone (bottom panels). For instance, from the bottom panel of mode ν_2 [Fig. 6(b)], the large arrows on the benzene Hydrogen atoms might suggest they play an important role in the generation of the inelastic signal. When the distribution of the transmission eigenchannels (Fig. 1) is taken into account, however, the role of these H atoms is diminished and the C atoms on the conjugated ring emerge as more relevant (top panel).

The modes in Fig. 6 are characterized by a relatively low cancellation parameter ($\delta \simeq 0.13$). The real-space mapping of local contributions shows that these add constructively in both cases, which results in these modes having a relatively high inelastic signal.

On the other hand, the inelastic signal for modes ν_3 and ν_4 (Fig. 7) is almost zero. For both of these dark modes, the cancellation parameter is very high (0.99 in both cases). Analysis of the local contribution pattern reveals that the different terms tend to cancel each other out. Notice from scale of the color bar that the magnitude of the individual contributions is much larger than the total sum γ_{tot}. This pair-wise cancellation pattern prevents the modes from giving an appreciable signal and thus we classify both modes as dark.
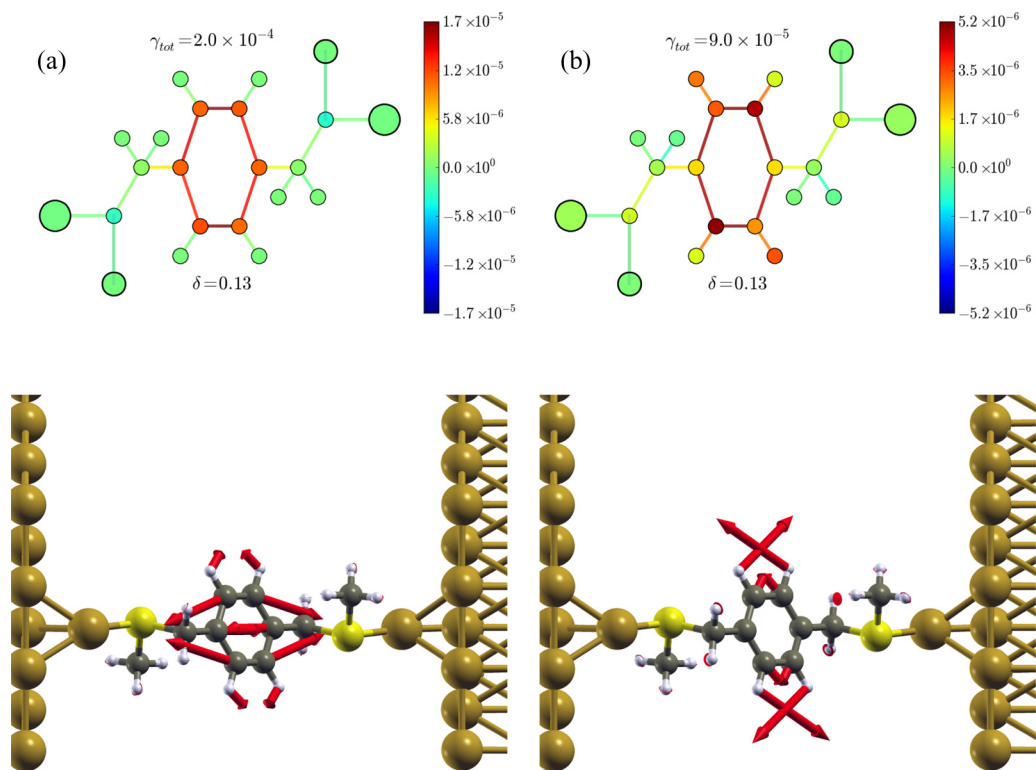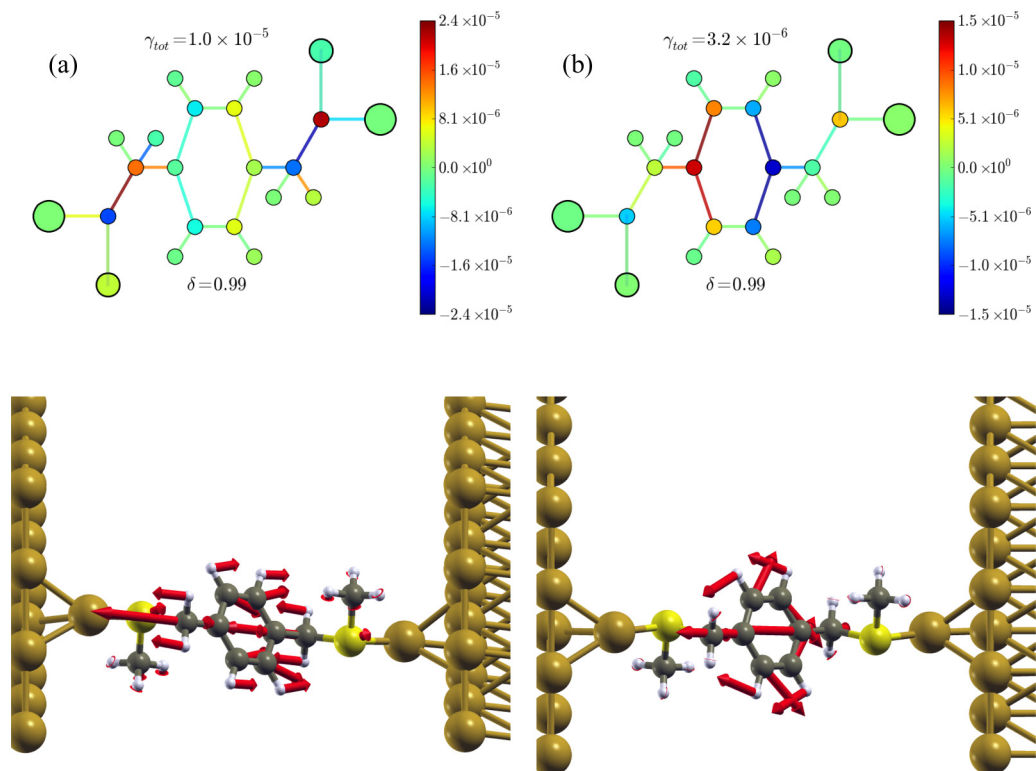
FIG. 6. Sketch of the adatom-molecule-adatom complex showing the local contributions (top panels) and visualization of the vibrational modes (bottom panels) for active modes (a) ν_1 and (b) ν_2.

FIG. 7. Sketch of the adatom-molecule-adatom complex showing the local contributions (top panels) and visualization of the vibrational modes (bottom panels) for dark modes (a) ν_3 and (b) ν_4.
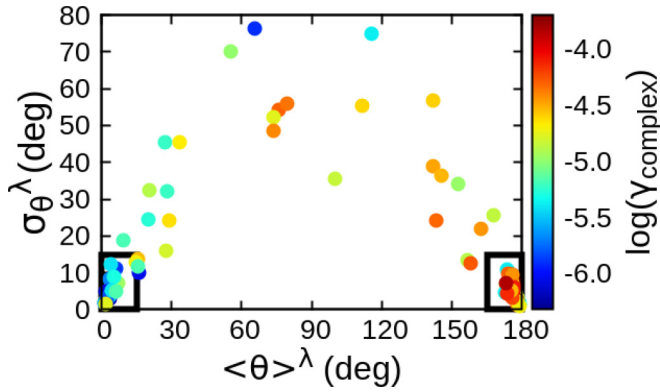
FIG. 8. Characterization of the degree of symmetry of vibrational modes: standard deviation of the angles between $\vec{v}_\alpha^\lambda$ and $\vec{v}_{\alpha'}^\lambda$ on chemically equivalent atoms as a function of the mean angle for each mode. The color bar shows the inelastic signal of that mode generated on the molecular complex.

D. Characterization of vibrational modes

We now seek to establish a general connection, across all vibrational modes, between the intensity of the inelastic signal and the geometrical structure of the mode. For this we consider pairs of atoms α, α' in the molecular complex that are structurally equivalent: both Au adatoms, the pair of S atoms, the C atoms in both CH_3 groups, and so on. For each mode we then calculate the standard deviation of the angles $\theta_{\alpha,\alpha'}^\lambda$ between the components $\vec{v}_\alpha^\lambda$ and $\vec{v}_{\alpha'}^\lambda$ of the $\mathbf{v}^\lambda$ vectors on these pairs of chemically equivalent atoms:

$$\sigma_\theta^\lambda = \sqrt{\frac{1}{N} \sum_\alpha \left(\theta_{\alpha,\alpha'}^\lambda - \langle\theta\rangle^\lambda\right)^2}, \qquad (7)$$

where the sum runs over pairs of equivalent atoms on the molecular complex, N is the number of such pairs, and $\langle\theta\rangle^\lambda$ is the mean value of the angles for a given mode. The mean value and standard deviation thus give a measure of the degree of (a)symmetry of the mode from the magnitude and direction of the components of $\mathbf{v}^\lambda$ on each pair of equivalent atoms.

Figure 8 characterizes the degree of symmetry of vibrational modes. Each point corresponds to one vibrational mode. The color bar represents the magnitude of the inelastic contribution generated on the molecular complex. When $\langle\theta\rangle^\lambda \simeq 0°$ the vectors $\vec{v}_\alpha^\lambda$ and $\vec{v}_{\alpha'}^\lambda$ acting on the atoms are, on average, pointing in the same direction; these modes have a strong antisymmetric character. On the other hand, when $\langle\theta\rangle^\lambda \simeq 180°$, the $\vec{v}_\alpha^\lambda$ and $\vec{v}_{\alpha'}^\lambda$ vectors acting on pair of chemically equivalent atoms point in opposite directions; these modes have a strong symmetric character. From the value of σ_θ^λ and $\langle\theta\rangle^\lambda$ we can identify three types of vibrational modes. Around $\langle\theta\rangle^\lambda = 0°$ and $\langle\theta\rangle^\lambda = 180°$ there is an accumulation of points with a low standard deviation, indicating that some modes have a strong symmetric or antisymmetric character. The accumulation of blue (red) data points near $\langle\theta\rangle^\lambda \simeq 0°$ ($\langle\theta\rangle^\lambda \simeq 180°$) reveals a general trend where modes with $\langle\theta\rangle^\lambda \simeq 0°$ ($\langle\theta\rangle^\lambda \simeq 180°$) have a weak (strong) inelastic signal. This is highlighted by the black rectangles in Fig. 8 defined by the small (though admittedly arbitrary) values $\langle\theta\rangle_{\max}^\lambda = 15°$ and $\sigma_{\theta,\max}^\lambda = 15°$.

Figure 8 shows that many modes do not have a mean angular value close to $0°$ or $180°$. These modes also have values of σ_θ^λ indicative of a large dispersion in the angles across the different pairs of equivalent atoms in each mode. Thus, they do not present a clear symmetric or antisymmetric character.

We find that these modes are characterized by a more pronounced motion of the atoms on only one side of the molecule, typically on one of the two CH_3 groups. Modes ν_5 and ν_6 fall into this third category and Fig. 9 shows the associated local contribution pattern.

This analysis of the angular distribution of the vibrational modes thus establishes a connection between the direction of the components of $\mathbf{v}^\lambda$ (eigenvectors of the dynamical matrix) on pairs of chemically equivalent atoms and the intensity of the inelastic signal. Modes for which $\vec{v}_\alpha^\lambda$ and $\vec{v}_{\alpha'}^\lambda$ point, on average, in opposite directions, tend to give a strong inelastic signal while modes where $\vec{v}_\alpha^\lambda$ and $\vec{v}_{\alpha'}^\lambda$ point in the same direction are, in general, dark. However, it is worth mentioning that many modes do not fit into either of these categories. The inelastic signal of modes in this third category, typically modes involving one of the two CH_3 groups more than the other, spans a wide range of values. We discussed in Sec. II B how modes with a low (high) cancellation parameter δ resulted in a strong (weak) inelastic signal γ_{tot}, as expected. However, the inverse statement is not necessarily true: many modes yielding a relatively high inelastic peak have intermediate values of δ (0.5–0.7, Fig. 4). Modes in this third category are usually asymmetric and thus the inelastic contributions of one part of the molecule can only partially add to or cancel the contributions of the other part of the molecule. This results in intermediate values of δ and a wide range of values of γ_{tot}.

Previous works relating the intensity of the inelastic signal to the symmetry of vibrational modes [23–25] have explored the propensity rules for relatively simple systems with a high symmetry. However, a more quantitative characterization of the symmetry of all vibrational modes enables the extension of the analysis to the more general case of complex molecular structures with no well-defined symmetries of the modes. In order to get further insight into the quantitative connection between the spatial symmetry of the modes and the intensity of the inelastic signal for a general case, we define the following symmetry parameter for each vibrational mode:

$$S_\lambda = \frac{1}{N} \sum_\alpha A_{\alpha,\alpha'}^\lambda P_{\alpha,\alpha'}^\lambda, \qquad (8)$$

where

$$A_{\alpha,\alpha'}^\lambda = \frac{|\vec{v}_\alpha^\lambda| + |\vec{v}_{\alpha'}^\lambda|}{2|\vec{v}^\lambda|_{\max}}, \qquad (9)$$

$$P_{\alpha,\alpha'}^\lambda = \cos(\theta)\left(1 - \frac{||\vec{v}_\alpha^\lambda| - |\vec{v}_{\alpha'}^\lambda||}{\max(|\vec{v}_\alpha^\lambda|, |\vec{v}_{\alpha'}^\lambda|)}\right). \qquad (10)$$

As before, α and α' are pairs of chemically equivalent atoms on the molecular complex and N is the number of such pairs. The prefactor $A_{\alpha,\alpha'}^\lambda$ in Eq. (9) measures the importance of the α, α' pair in the mode by scaling the vectors on those atoms to the maximal value in the mode. Pairs with smaller vectors in the representation of the vibrational mode (Figs. 6, 7, and 9, lower panels) will contribute less to S_λ of that mode.

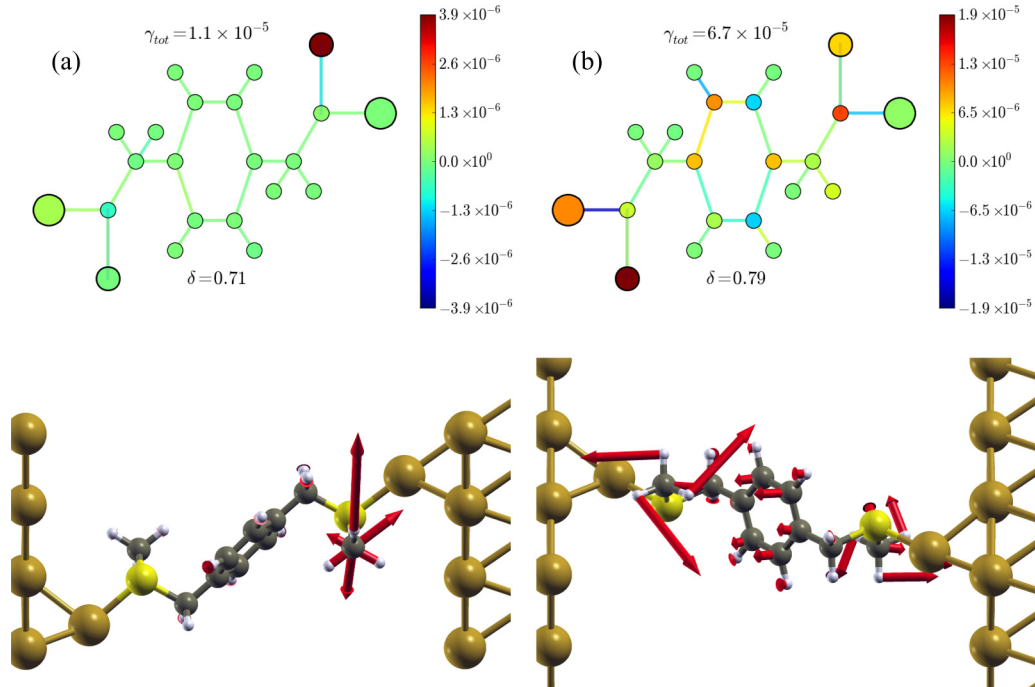FIG. 9. Local contribution plots (top panels) and visualization of the vibrational modes (bottom panels) for asymmetric modes (a) ν_5 and (b) ν_6.

The term $P_{\alpha,\alpha'}^{\lambda}$ in Eq. (10), on the other hand, measures the amplitude of the vibrational mode on atoms α and α' and the direction of these vibrations (through $\cos\theta$). For each mode, the quantity S_λ is the result of the weighted average over all pairs of equivalent atoms in the adatom-molecule-adatom complex. If, for a given mode, the movement on all pairs were in opposite directions ($\cos\theta = -1$) and had equal amplitudes pairwise ($|\vec{v}_\alpha^\lambda| = |\vec{v}_{\alpha'}^\lambda|$), then the mode would be perfectly symmetric and $S_\lambda = -1$. If, on the other hand, the mode moved equivalent pairs of atoms in the same direction ($\cos\theta = 1$) and with the same amplitude ($|\vec{v}_\alpha^\lambda| = |\vec{v}_{\alpha'}^\lambda|$), the mode would be perfectly antisymmetric and $S_\lambda = 1$. Modes where the amplitude on one atom is different to that on the equivalent atom ($|\vec{v}_\alpha^\lambda| \neq |\vec{v}_{\alpha'}^\lambda|$) are neither symmetric nor antisymmetric and result in intermediate values of S_λ between -1 and 1 depending on how big this difference is and on how relevant this pair of atoms is in the vibrational mode ($A_{\alpha,\alpha'}^\lambda$). For the molecular system studied, we find many modes in this third category.

Figure 10 shows the inelastic signal generated on the adatom-molecule-adatom complex $\gamma_{complex}$ as a function of the symmetry parameter S_λ. First, one can notice that, for a realistic system like the one we are considering, S_λ never reaches ± 1, which means that no mode is perfectly symmetric or antisymmetric. Also, although the data show some dispersion, we can clearly see a trend in which (symmetric) modes with a negative S_λ show a strong inelastic signal $\gamma_{complex}$ and (antisymmetric) modes with positive S_λ have a weak signal. In the central part of the plot there are many modes with a low spatial symmetry and small values of S_λ and an intermediate inelastic signal: the local contributions from one part of the molecular complex cannot fully add up with or cancel out the ones in the equivalent part of the complex, yielding a relatively

low-cancellation parameter δ, small S_λ, and a nonzero inelastic signal.

E. Breaking the symmetry of the cancellation pattern: Activating dark modes

Our analysis across all vibrational modes shows that, for dark modes, pair-wise cancellations on equivalent atoms of the molecule cancel each other out resulting in a very small inelastic signal. In this section we show how breaking the symmetry of the cancellation pattern of a dark mode results in the activation of the mode. We focus on a flat region of the spectrum where there is no signal and focus on the dark mode
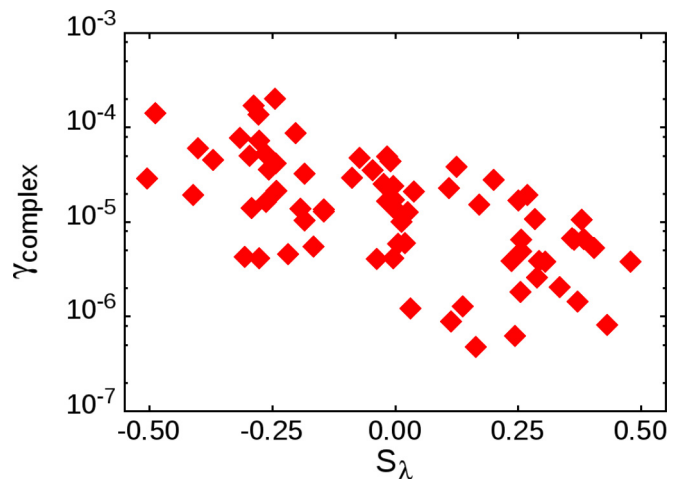

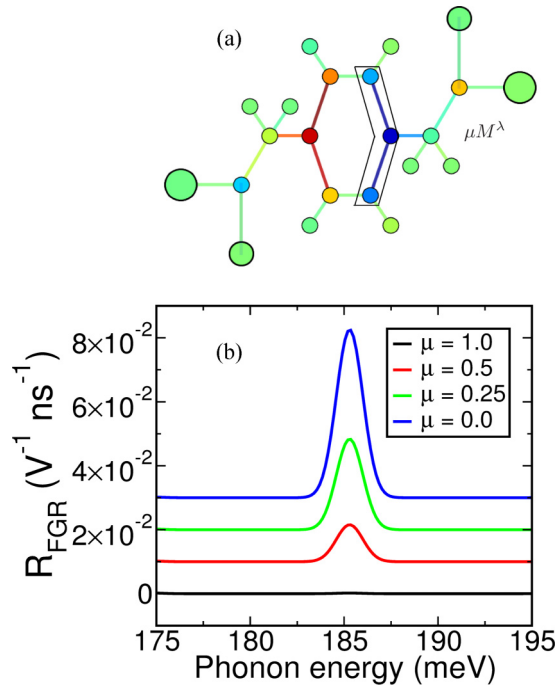FIG. 10. Inelastic signal $\gamma_{complex}$ as a function of the symmetry parameter S_λ.

FIG. 11. Gradual activation of a dark mode ν_3. (a) Real-space mapping of the local contributions on the molecular complex for mode ν_3. The polygon defines the region where the electron-phonon matrix elements are gradually quenched. (b) Inelastic rates R_{FGR}^λ for four different values of the parameter μ. The curves have been shifted vertically for clarity.

FIG. 12. Visualization of the vibrational modes at (a) 368 meV and (b) 381 meV.

ν_3 where the cancellation pattern leads to a δ value close to 1 and $S_\lambda = 0.29$ (Table I).

We gradually switch to zero the electron-phonon coupling matrix elements in Eq. (1) and compute the changes in the inelastic spectrum. We do this by introducing a parameter μ, which multiplies the electron-phonon coupling matrix elements of three of the benzene C atoms [Fig. 11(a)]. Initially, $\mu = 1$, there is no perturbation [black curve, Fig. 11(b)] and the mode is dark. As the value of μ is decreased, the electron-phonon elements of these C atoms are quenched. The cancellation pattern is progressively broken and a peak emerges from the formerly dark mode [Fig. 11(b)]. This activation of a dark mode, illustrated here for the antisymmetric mode ν_3, can be applied to any other mode.

F. High-energy modes: Role of metal-molecule coupling

As we discussed, considering only the inelastic contributions generated in the adatom-molecule-adatom complex is a good approximation for most vibrational modes [Fig. 3(a)]. However, there are exceptions where including the contributions from the Au layers is necessary, such as the modes around 170, 368, and 381 meV.

Here we focus on the two modes that give the highest inelastic signal (at 368 and 381 meV) and use a similar analysis to study the role of the Au surface atoms in the intensity of these high-energy modes. These modes are characterized by the movement of the CH_3 groups (Fig. 12). Due to the proximity to the Au surface layers, the movement defined by the vibrational modes results in a modulation of the electronic coupling
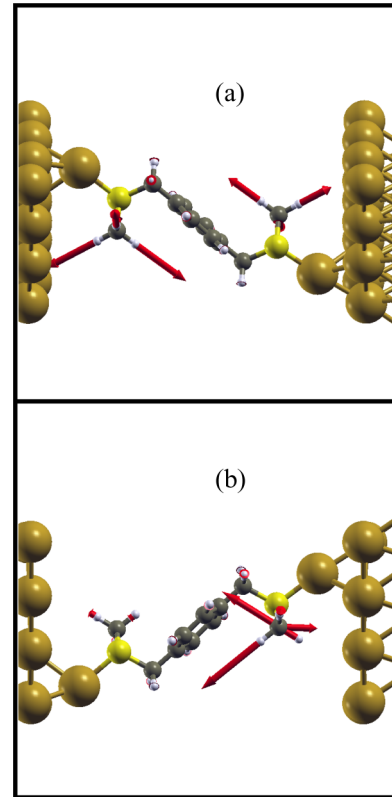
between CH_3 and surface layer orbitals. As a consequence, contributions involving Au surface atoms are relevant for these high-energy peaks.

For each mode we identify which surface atoms gives the strongest contributions to the inelastic peaks. We calculate the contribution of atom α as the sum:

$$\gamma_\alpha = \gamma_{\alpha,\alpha} + \sum_{\beta,\beta \neq \alpha} (\gamma_{\alpha,\beta} + \gamma_{\beta,\alpha}), \tag{11}$$

where we include both rows and columns in the electron-phonon coupling matrix ($\gamma_{\alpha,\beta}$, $\gamma_{\beta,\alpha}$) to account for all interactions derived from atom α. This ensures that the values of Eq. (11) corresponding to different atoms are comparable. In Figs. 13(a) and 13(b) the Au surface atoms, which give the strongest contributions for these modes, are highlighted in blue. The terminal S-CH_3 fragments of the molecule are shown for clarity. As before, we calculate the inelastic signal gradually quenching the electron-phonon coupling matrix elements of the Au atoms highlighted in blue in Fig. 13 through the μ parameter. $\mu = 1$ represents the initial situation [no perturbation, black curve in Fig. 13(c)], while $\mu = 0$ (blue curve) corresponds to the case where these matrix elements have been completely switched off. The peaks at 372 and 386 meV, which are given mostly by the contributions on the molecular complex, remain unchanged in the process. As the value of μ is decreased and the contributions from these selected Au atoms are quenched, the peaks at 368 and 381 meV are significantly reduced. Notice that the vibrational modes do not involve movement of Au surface atoms as
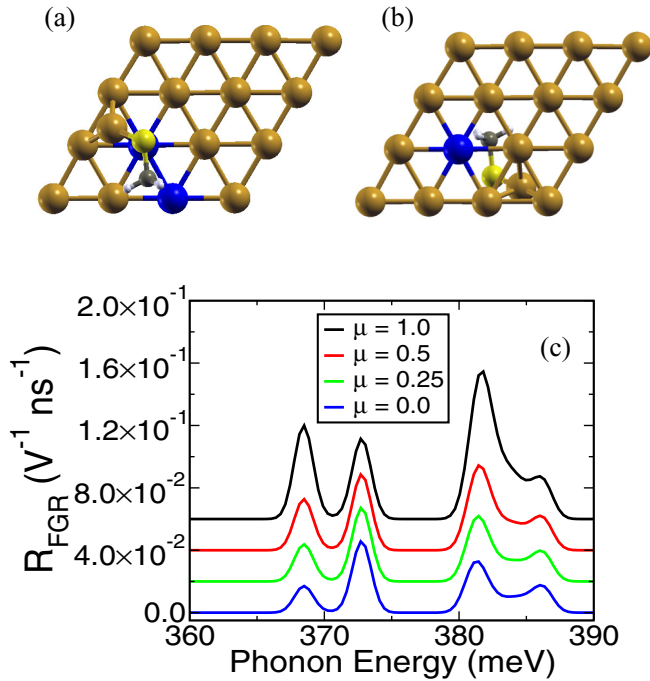
FIG. 13. View of the bottom (a) and top (b) Au surface layers and terminal S-CH$_3$ groups. The Au atoms with the largest contributions to the modes at 368 and 381 meV are highlighted in blue. (c) Inelastic rates R$_{FGR}^\lambda$ obtained by gradually quenching the contributions coming from these surface atoms highlighted in blue.

they are not included in the dynamical region. Instead, these atoms contribute through their electronic coupling to the CH$_3$ groups. This exemplifies the usefulness of this analysis as it allows for the identification of specific surface atoms giving the most important contributions to the high-energy modes and to quantify their contribution.

IV. CONCLUSIONS

We have presented an approach to explore the origin and intramolecular contributions of the inelastic tunneling signal of molecular junctions. In a local-orbital picture, we decomposed the total signal by grouping the different terms according to the atoms involved in each contribution. We carried out this study using DFT and analyzed all 84 vibrational modes of a representative benzene-based molecular junction with a low degree of symmetry.

These local contributions that make up the inelastic signal combine the information on the electronic structure present in the scattering channels with the geometric information of the vibrational modes and open the way to a series of results on the complex pattern behind the generation of IETS signal. The real-space representation of the local inelastic contributions allows for the mapping of the contribution of each atom and bond to every vibrational mode. Not surprisingly, modes where different contributions add up with the same sign result in a strong signal, while modes where these contributions cancel each other out result in dark modes. For this generic molecule, however, we find that in most modes there is a large number of (partial or total) cancellations between the different local contributions. By studying on the contributions of chemically equivalent atoms, we could identify a pattern of pair-wise additions or cancellations leading to a quantitative connection between the symmetry of the vibrational mode and the strength of the inelastic signal. Modes where chemically equivalent atoms move in opposite directions (symmetric modes) are active while those where chemically equivalent atoms move in the same direction (asymmetric modes) are dark. However, for the generic molecule studied, many modes do not have a clear symmetry and it was necessary to develop a new parameter S_λ to quantify the degree of symmetry of the mode. This new symmetry parameter shows a clear relation with the intensity of the inelastic signal. Finally, we illustrated how this analysis can identify the most important atoms contributing to IETS peaks and showed examples of how perturbing the local contributions by gradually quenching the electron-phonon matrix elements can change the IETS signal. In one example this quenching leads to the activation of a dark mode, while in the other example it leads to a decrease of the inelastic signal. In summary, the analysis of the local contributions provides a quantitative relation of the degree of symmetry of vibrational modes and their inelastic signal, a real-space picture of the pattern of addition and cancellation of local contributions and opens the way to the controlled modification of the inelastic spectrum.

[1] D. Walmsley, I. McMorris, and N. Brown, Solid State Commun. **16**, 663 (1975).

[2] Y. Kim, T. Komeda, and M. Kawai, Phys. Rev. Lett. **89**, 126104 (2002).

[3] J. I. Pascual, N. Lorente, Z. Song, H. Conrad, and H.-P. Rust, Nature **423**, 525 (2003).

[4] C.-l. Chiang, C. Xu, Z. Han, and W. Ho, Science **344**, 885 (2014).

[5] R. C. Jaklevic and J. Lambe, Phys. Rev. Lett. **17**, 1139 (1966).

[6] B. C. Stipe, M. A. Rezaei, and W. Ho, Science **280**, 1732 (1998).

[7] B. C. Stipe, M. A. Rezaei, and W. Ho, Phys. Rev. Lett. **82**, 1724 (1999).

[8] W. Ho, J. Chem. Phys **117**, 11033 (2002).

[9] R. H. M. Smit, Y. Noat, C. Untiedt, N. D. Lang, M. C. van Hemert, and J. M. van Ruitenbeek, Nature **419**, 906 (2002).

[10] W. Wang, T. Lee, I. Kretzschmar, and M. A. Reed, Nano Lett. **4**, 643 (2004).

[11] M. A. Reed, Materials Today **11**, 46 (2008).

[12] N. Okabayashi, M. Paulsson, H. Ueba, Y. Konda, and T. Komeda, Phys. Rev. Lett. **104**, 077801 (2010).

[13] Y. Kim and H. Song, Appl. Spectrosc. Rev. **51**, 603 (2016).

[14] B. N. J. Persson and A. Baratoff, Phys. Rev. Lett. **59**, 339 (1987).

[15] T. Mii, S. G. Tikhodeev, and H. Ueba, Phys. Rev. B **68**, 205406 (2003).

[16] M. Galperin, M. A. Ratner, and A. Nitzan, J. Chem. Phys **121**, 11965 (2004).

[17] M. Paulsson, T. Frederiksen, H. Ueba, N. Lorente, and M. Brandbyge, Phys. Rev. Lett. **100**, 226604 (2008).

[18] J. K. Viljas, J. C. Cuevas, F. Pauly, and M. Häfner, Phys. Rev. B **72**, 245415 (2005).

[19] T. Frederiksen, M. Paulsson, M. Brandbyge, and A.-P. Jauho, Phys. Rev. B **75**, 205413 (2007).

[20] A. Gagliardi, G. Romano, A. Pecchia, A. D. Carlo, T. Frauenheim, and T. A. Niehaus, New J. Phys. **10**, 065020 (2008).

[21] H. Nakamura, K. Yamashita, A. R. Rocha, and S. Sanvito, Phys. Rev. B **78**, 235420 (2008).

[22] M. Bürkle, J. K. Viljas, T. J. Hellmuth, E. Scheer, F. Weigend, G. Schön, and F. Pauly, Phys. Status Solidi (b) **250**, 2468 (2013).

[23] N. Lorente, M. Persson, L. J. Lauhon, and W. Ho, Phys. Rev. Lett. **86**, 2593 (2001).

[24] A. Troisi and M. A. Ratner, Nano Lett. **6**, 1784 (2006).

[25] A. Gagliardi, G. C. Solomon, A. Pecchia, T. Frauenheim, A. Di Carlo, N. S. Hush, and J. R. Reimers, Phys. Rev. B **75**, 174306 (2007).

[26] A. Garcia-Lekue, D. Sanchez-Portal, A. Arnau, and T. Frederiksen, Phys. Rev. B **83**, 155417 (2011).

[27] Z. Jiang, H. Wang, S. Sanvito, and S. Hou, J. Chem. Phys. **143**, 234709 (2015).

[28] D. J. Mowbray, G. Jones, and K. S. Thygesen, J. Chem. Phys. **128**, 111103 (2008).

[29] H. Song, Y. Kim, Y. H. Jang, H. Jeong, M. A. Reed, and T. Lee, Nature **462**, 1039 (2009).

[30] M. Dell'Angela, G. Kladnik, A. Cossaro, A. Verdini, M. Kamenetska, I. Tamblyn, S. Y. Quek, J. B. Neaton, D. Cvetko, A. Morgante, and L. Venkataraman, Nano Lett. **10**, 2470 (2010).

[31] Y. Kim, T. Pietsch, A. Erbe, W. Belzig, and E. Scheer, Nano Lett. **11**, 3734 (2011).

[32] J.-T. Lü, R. B. Christensen, G. Foti, T. Frederiksen, T. Gunst, and M. Brandbyge, Phys. Rev. B **89**, 081405 (2014).

[33] H. Vázquez, R. Skouta, S. Schneebeli, M. Kamenetska, R. Breslow, L. Venkataraman, and M. Hybertsen, Nat. Nanotechnol. **7**, 663 (2012).

[34] J. M. Soler, E. Artacho, J. D. Gale, A. García, J. Junquera, P. Ordejón, and D. Sánchez-Portal, J. Phys.: Condens. Matter **14**, 2745 (2002).

[35] M. Brandbyge, J.-L. Mozos, P. Ordejón, J. Taylor, and K. Stokbro, Phys. Rev. B **65**, 165401 (2002).

[36] J. P. Perdew, K. Burke, and M. Ernzerhof, Phys. Rev. Lett. **77**, 3865 (1996).

[37] G. Foti, D. Sánchez-Portal, A. Arnau, and T. Frederiksen, Phys. Rev. B **91**, 035434 (2015).

[38] M. Paulsson and M. Brandbyge, Phys. Rev. B **76**, 115117 (2007).

[39] M. Paulsson, T. Frederiksen, and M. Brandbyge, Phys. Rev. B **72**, 201101 (2005).

[40] H. Song, Y. Kim, J. Ku, Y. H. Jang, H. Jeong, and T. Lee, Appl. Phys. Lett. **94**, 103110 (2009).

[41] C. R. Arroyo, T. Frederiksen, G. Rubio-Bollinger, M. Vélez, A. Arnau, D. Sánchez-Portal, and N. Agraït, Phys. Rev. B **81**, 075405 (2010).